Applied Physics A (2019) 125:162
https://doi.org/10.1007/s00339-019-2450-y

Applied Physics A
Materials Science & Processing

One-step green synthesis of WO_3 nanoparticles using *Spondias mombin* aqueous extract: effect of solution pH and calcination temperature

J. O. Tijani[1,3] · O. Ugochukwu[1,3] · L. A. Fadipe[1] · M. T. Bankole[1,3] · A. S. Abdulkareem[2,3] · W. D. Roos[4]

Received: 19 December 2018 / Accepted: 28 January 2019

Abstract
In this study, a novel green synthesis of tungsten trioxide (WO_3) nanoparticles from ammonium paratungstate, $(NH_4)_{10}W_{11}O_{41}{\cdot}5H_2O$) and aqueous leaves extract of *Spondias mombin* was explored. The effect of solution pH (1, 4, 7,10, 13) and calcination temperature (250°, 350°, 450°, 550°, 650 °C) on the morphological characteristics and surface area of the nanoparticles were examined. The prepared WO_3 nanoparticles were characterized using High-Resolution Scanning Electron Microscopy (HRSEM), Energy-Dispersive X-ray Spectroscopy (EDX), X-ray Diffraction (XRD), Brunauer Emmett and Teller (BET), and X-ray Photoelectron Spectroscopy (XPS). The HRSEM analysis showed the formation of highly dispersed less agglomerated spherical-shaped structures at each studied pH and calcination temperature except at pH 13. The particle size of the WO_3 nanoparticles increased with increase in pH in the order of $13.8 < 14.3 < 16.7 < 17.6$ nm for pH 1, 4, 7, and 10, respectively. While there was no evidence of formation of WO_3 nanoparticles of definite size at pH 13. XRD patterns confirmed the existence of only monoclinic phase of WO_3 irrespective of the solution pH and calcination temperature with average crystallite sizes of about 27.14 nm, 14.39 nm, and 5.90 nm at pH 1, 3, and 5, respectively. The BET analysis established that as-synthesized samples had higher surface area (352.59 m^2/g) at pH 1 and calcination temperature (550 °C) than a commercial available WO_3 (19.42 m^2/g). It was also found that the specific surface area of the samples decreased from 352.59 to 223.67 m^2/g, as the solution pH increased from 1 to 10. While for calcination temperature over the range of 250–650 °C, the surface area increased from 156.34 to 352.59 m^2/g. XPS demonstrated the presence of W atom in the oxidation state of +6 and lattice oxygen as O^{2-}. The facile green route to prepared WO_3 nanoparticles was accomplished and calcination temperature and solution pH play crucial role on the shape, size, and surface area of the material.

1 Background

Tungsten (VI) oxide (WO_3) nanoparticles have attracted special interests in the field of photocatalysis among researchers due to its strong adsorption within the solar spectrum ($\leq$500 nm), stable physico-chemical properties, as well as its resilience to photo-corrosion [33, 53]. Nanostructured tungsten trioxide (WO_3) is a semiconductor metal oxide with a bandgap of between 2.4 and 2.8 eV and exhibits a cubic perovskite-like structure based on the corner sharing of regular octahedral with the O atoms at the corner and the W atom at the center of each octahedron [39]. The remarkable feature of crystalline WO_3 is its various polymorphs, such as triclinic [15], monoclinic [23], orthorhombic [54], tetragonal [11], hexagonal [36], and cubic [54]. Other phases include mixed crystal frameworks, such as monoclinic–tetragonal [50], monoclinic–triclinic [25], monoclinic–hexagonal [28], orthorhombic–hexagonal [27], orthorhombic–monoclinic [40], and orthorhombic–cubic [4]; Most of these crystalline phases exhibit excellent photocatalytic activity under visible light [3].

Several methods sol–gel [23], acidification [44], chemical vapour deposition [30, 46], low-temperature hydrothermal

✉ J. O. Tijani
jimohtijani@futminna.edu.ng

[1] Department of Chemistry, Federal University of Technology, PMB. 65, Minna, Niger State, Nigeria

[2] Department of Chemical Engineering, Federal University of Technology, PMB. 65, Minna, Niger State, Nigeria

[3] Nanotechnology Research Group, Centre for Genetic Engineering and Biotechnology (CGEB), Federal University of Technology, P.M.B 65, Bosso, Minna, Niger State, Nigeria

[4] Department of Physics, University of the Free State, P.O. Box 339, Bloemfontein 9300, Republic of South Africa

Published online: 05 February 2019

method [47], solid-state sintering method [16], microwave-assisted hydrothermal method [18, 42], co-precipitation [29], urea-assisted combustion [52], spray pyrolysis [31], hydrothermal [21], electrodeposition [5], template-assisted growth method [41], thermal evaporation [24], electrospinning [34], and pulsed laser deposition [12] have been employed to synthesize WO_3 nanomaterials. The preparation procedure of nanoparticles through conventional physical and chemical methods is complicated, time consuming, generates toxic byproducts, and is costly [7]. Tungsten (VI) oxide, also known as tungsten trioxide or tungstic anhydride, can equally be deposited in the form of thin films using various deposition techniques and can be used for diverse scientific and technological applications [17]. Each deposition technique produced different properties on different substrates in terms of composition, structure, and morphology [14]. Researchers have employed different methods to prepare WO_3 nanoparticles. For instance, Aminian [2] synthesized WO_3 nanoparticles using peroxo tungstic acid solution as a precursor via hydrothermal and precipitation methods and calcined cake obtained at 500 °C for 2 h. The prepared material nanoparticles, nanorods, and nanosheets were characterized by XRD, UV–Vis, SEM, and BET and found that the samples composed of nanostructures with an average lateral thickness of 20–47 nm. Wicaksana et al. [49] synthesized WO_3 nanobundles, nanocubes, and nanoparticles using hydrothermal method at 200 °C for 10 h. The samples were characterized using ICP-AEC, SEM, BET, UV–Vis, and XPS and the results showed particle size between 100 and 200 nm, surface area in the range of (8.3–44.4 m^2/g) for the monoclinic- and orthorhombic-phased nanomaterials. Vamvasakis et al. [47] employed combination of sol–gel and precipitation methods followed by hydrothermal treatment to synthesize WO_3 nanoparticles. The authors examined the influence of synthesis method and calcination temperature and found that the surface area and morphological characteristics were dependent on the nature of the tungsten precursors.

In recent years, there has been growing interest in the synthesis of nanoparticles through environmentally benign protocol that utilizes plant extracts or microbes than conventional physical and chemical methods. In this case, the extract is simply mixed with a solution of the metal precursor at room temperature and the reaction is usually complete within minutes [32]. The same methods have been used in the production of silver, gold, palladium, and many other metal nanoparticles [22]. The nature of the plant extract, its concentration, the concentration of the metal salt, the pH, temperature, and stirring time are known to affect the rate of production of the nanoparticles, their quantity, and other characteristics [10]. This method is considered more economical, energy saving, and eco-friendly and does not require complex procedures [22]. The review of available literature showed that there is little or no information on the green synthesis of WO_3 using plant extracts and optimization of solution pH and calcination temperatures on the shape and size of WO_3 nanoparticles has not been thoroughly investigated. The plant *Spondias mombin* is a fructiferous tree that belongs to the family Anacardiacae and grows in the coastal areas, typically rain forest into a big tree of up to 15–22 m in height. It is commonly available in Nigeria, Brazil, and several other tropical forests of the world with high genetic variability among populations. All parts of the tree are ethno-pharmacologically important. Phytochemical screening of *Spondias mombin* extract revealed the presence of alkaloids, reducing sugars, cardiac glycosides, flavonoids, tannins, saponins, steroids, and terpenoids [1, 35]. To the best of the authors' knowledge, this is the first green synthesis of WO_3 nanoparticles, where aqueous leaf extract of *Spondias mombin* aqueous was explored as reducing, capping, and stabilizing agent. The structural, morphological, surface chemical oxidation states, and surface area of the as-synthesized WO_3 nanoparticles were examined.

2 Experimental section

2.1 Materials

$(NH_4)_{10}W_{12}O_{41}{\cdot}5H_2O$ (98%), NH_4OH (24.01%), and HNO_3 (70.3%) were supplied by Sigma-Aldrich (USA). All chemicals and reagents were used without any further purification. Fresh leaves of *Spondias mombin* (Plum Hog) were randomly collected from Bida, Niger State, washed, sun dried in the open air for a week, and crushed to a fine powder using a mechanical blender.

2.2 Extraction of *Spondias mombin* extract

Powdered leaves of *Spondias mombin* (50 g) were refluxed with 400 cm^3 of distilled water for 2 h. The resulting mixture was filtered using Whatman No 1 filter paper and the filtrate concentrated and dried over a water bath at 50 °C. The dried extract was weighed, placed in a sterile bottle, and labelled aqueous extract of *Spondias mombin*. This extract was used both as a reducing and stabilizing agent for the preparation of the WO_3 nanoparticles from the ammonium paratungstate $(NH_4)_{10}W_{12}O_{41}{\cdot}5H_2O$ precursor.

2.3 Qualitative and quantitative screening of *Spondias mombin* extract

The extract was subjected to phytochemical (qualitative) screening for the presence of flavonoids, tannins, and total phenols using standard methods. The quantity of these secondary metabolites in the aqueous extract of *Spondias*

mombin was further determined using established standard procedures. The Folin–Ciocalteau method was used to determine the total phenolic content [8], while quantity of flavonoids and Tannins was both determined by method described by Chang et al. [6].

2.4 Green synthesis of WO_3 nanoparticles

A known volume (10 cm^3) of aqueous leaf extract of *Spondias mombin* (see Fig. 1a) was added slowly to 100 cm^3 of 0.06 M ammonium paratungstate solution (see Fig. 1b). The mixture was gently heated at 120 °C under continuous stirring at 150 rpm for about 30 min. Subsequently, 10% HNO_3 was added drop wisely to adjust pH value to acidic range between 1 and 4, while 0.5 M NH_4OH was added to increase the pH to between 7, 10, and 13. The solution was further stirred for 30 min. A change in colour from rusty brown to yellow (see Fig. 1c) accompanied the formation of white precipitates, as shown in Fig. 2d. The resultant solution was allowed to age for 24 h after which the white precipitate was separated from the aqueous extract, first by decantation, and then washed severally to remove any residual aqueous extract or impurities (Fig. 1e). The resultant white precipitate obtained under the applied conditions was dried at 80 °C in a moisture extractor for 6 h (see Fig. 1f). The obtained WO_3 cake was annealed at 550 °C in a furnace under air environment for 2 h. The step-by-step procedure used to prepare WO nanoparticles is presented in Fig. 1.

2.5 Effect of calcination temperature on the size and morphology

The effect of calcination temperature on the size and shapes of WO_3 nanoparticles was investigated by subjecting the as-prepared WO_3 nanoparticles to different temperatures from 250 °C, 350 °C, 450 °C, 550 °C, and 650 °C in the furnace for 2 h each.

2.6 Characterization of the as-synthesized WO_3 nanoparticles

The morphology, microstructure, and elemental composition of the as-synthesized WO_3 nanoparticles were determined using a Zeiss Auriga High-Resolution Scanning Electron Microscope and High-Resolution Transmission Electron Microscope (HRTEM) coupled with Energy-Dispersive Spectroscopy (EDS). Approximately 0.05 g of the each synthesized sample was sprinkled on a carbon tape which was fixed onto an aluminium stub. The HRSEM microscope was operated at 5 keV for imaging and 20 keV for EDS, while Zeiss Auriga HRTEM was operated at 200 kV. The mineralogical phase and the crystalline nature of the as-prepared WO_3 were examined using powder X-ray diffraction (XRD, Bruker D8 advance) operated under the following conditions: diffraction angle 2θ in the range of 20–90°, a step size of 0.028°, applied voltage 45 kV, applied current 40 mA, monochromatic radiation, and CuKα radiation with a wavelength of 0.154 nm was used as the X-ray source. The surface area of the as-synthesized WO_3

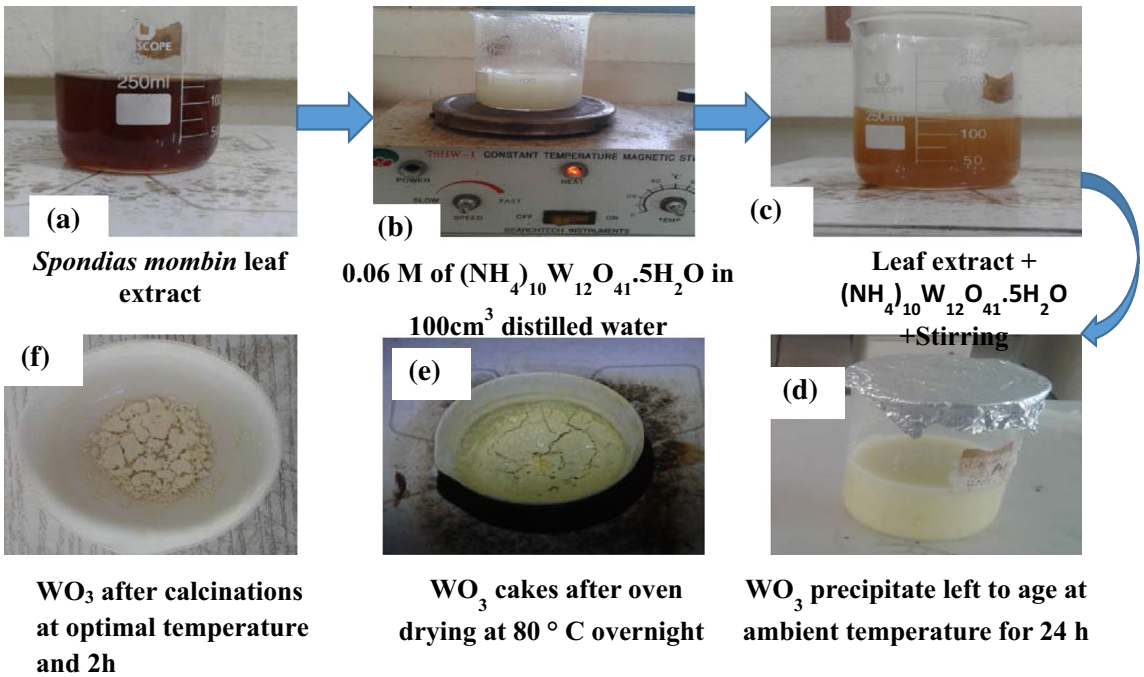

Fig. 1 Step-by-step green synthesis of WO_3 nanoparticles based on the variation of solution pH and calcination temperature

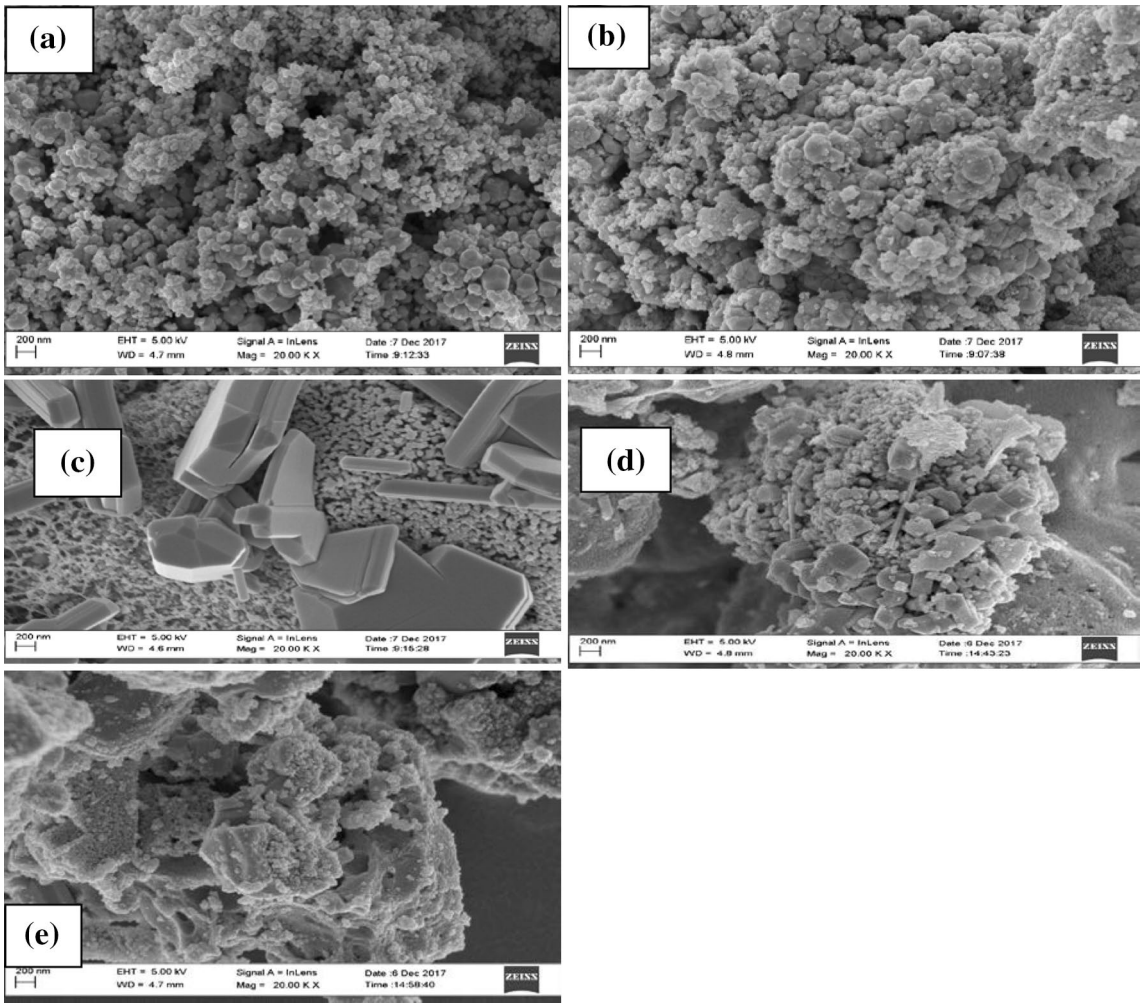

Fig. 2 HRSEM images of WO_3 nanoparticles at **a** pH 1, **b** pH 4, **c** pH 7, **d** pH 10, and **e** pH 13

nanomaterials was determined using nitrogen adsorption–desorption (NOVA 2400) at 77K in a Micromeritics ASAP2020 prior to degassing at 120 °C for 2 h to remove any residual impurities blocking the pores. The surface oxidation states of the synthesized nanomaterials were determined using X-ray Photoelectron Spectrometer (XPS PHI 5400) with an X-ray source of Mg Kα non-monochromatic and a photoelectron take-off angle for all measurements at 45° with a pass energy of 178.95 eV in steps of 0.5 eV and scan rate of 5 eV/s with no charge correction. High-resolution analyses were done with a pass energy of 44.75 eV, step size 0.125 eV, and scan rate of 0.625 eV/s. Charge correction was done by referencing to the adventitious carbon peak at 284.8 eV.

3 Results and discussion

As can be seen in Table 1, the amount of phenolic constituents in the aqueous leaves extract of *Spondias mombin* is high in the aqueous extract of *Spondias mombin*. This implies that the plant sample with greater amount of polyphenolic compounds can serve as stabilizing, reducing, and

Table 1 Qualitative and quantitative phytochemical screening of aqueous leaves extract of *Spondias mombin*

Phytochemical constituents	Qualitative	Quantitative (mg/ml)
Total flavonoids	+	0.9674
Total phenols	+++	13.0842
Total tannins	++	3.5022

+ present, ++ moderately, +++ highly present

capping agents for the green synthesis of WO_3 nanoparticles. This is evident in the formation of light brown coloration, as indicated in Fig. 2, after interaction with the tungsten precursor.

3.1 HRSEM analysis of the WO_3 nanoparticles synthesized at different pH

HRSEM was utilized for the structural and morphological properties of the as-synthesized WO_3 nanoparticles at different pH values (1, 4, 7, 10, and 13) and the images are shown in Fig. 2. The pH values were adjusted to the desired value using NaOH or HCl. The mechanism of formation of nanoparticles via variation of pH may be explained in terms of point of zero charge of WO_3. The point of zero of charge of WO_3 nanoparticles is 1.5, and below or above this value, there is an existence of attractive force between positive and negative particles, and as such, the particles collide with each other and aggregate and precipitate owing to van der Waals interaction. In the light of this background, at pH 1, well-defined agglomerated spherical shape with particle size in the range of 10–13 nm, which is similar to pure monoclinic phase. The formation of pure spherical shapes of the as-synthesized WO_3 nanoparticles at pH 1 may be due to strong electrostatic repulsion between hydroxonium ion and the tungsten salt precursor [49]. While at pH 4, a purely hexagonal shape was observed, while at pH 7, a mixture of hexagonal–spherical morphology, resembling monoclinic–orthorhombic phase, was formed, although the hexagonal morphology dominated. The particle sizes at pH 4 and 7 were in the range of 12–14 nm and 13–16.7 nm, respectively. The thick and large clusters observed at pH 7 may be linked to the coupling and aggregation of small particles during the aging process. At pH 10, a slight change in structure was observed, and agglomerated purely cuboid morphology corresponding to orthorhombic–hexagonal crystalline phase was formed with the particle sizes 14–17.6 nm. In contrast, no nanoparticle and phase transformation was noticed at pH 13 as confirmed by HRSEM analysis (Fig. 2e). In general, it was noticed that the particle size of the WO_3 nanoparticles increased with pH in the order of $13.8 < 14.3 < 16.7 < 17.6$ nm for pH 1, 4, 7, and 10, respectively.

A plausible explanation for the small particle size and spherical nature at low pH value may be attributed to the occurrence of super saturation reaction between the ammonium paratungstate and plant extract reacts to form paratungstate ions, such as $[W_{12}O_{41}]^{10-}$ and $[H_2W_{12}O_{40}]^{6-}$ in solution. The super saturation process was probably responsible for the homogeneous nucleation that generated large numbers of small WO_3 nuclei [48]. This nucleation, however, reduces as the solution pH increases resulting to the consumption of most of the tungsten precursor by the plant extract. Conversely, at pH 13, there was no occurrence of nucleation and coalescence mechanism, which is probably responsible for none-formation of the nanoparticles. Zhao and Miyauchi [53] found that the solution pH value influenced the morphology of WO_3 and acidic condition of pH of 5 favoured the formation of a tubular structure. In this study, the morphologies of the synthesized WO_3 nanoparticles were pH dependent. The observed morphological changes of WO_3 nanoparticles at different pH values support the findings of Zhao and Miyauchi [53] who observed cuboid to hexagonal morphology at pH 7 though without the addition of an acid or a base. While pure granular and spherical shapes corresponding to a monoclinic phase were observed at low pH of 1. In view of the small grain size and the pure monoclinic phase nature of the synthesized WO_3 nanoparticles, pH 1 was selected as the optimum.

3.1.1 HRSEM of WO_3 nanoparticles synthesized at different temperatures

The morphology of the WO_3 nanoparticles calcined in the furnace at temperatures between 250 and 650 °C at constant holding time of 2 h is represented in Fig. 3.

The HRSEM images of as-prepared WO_3 nanoparticles at a lower calcination temperature of 250 °C (Fig. 3a) reveal the formation of highly agglomerated small densely distributed WO_3 nanocrystals with no definite or irregular shape. The presence of small agglomerates of smaller size particles may be responsible for the porous morphology noticed in the HRSEM image (Fig. 3a). In addition, the observed morphology could be ascribed to the binding, capping, and stabilizing effects provided by biomolecules of *Spondias mombin* aqueous extract on the prepared WO_3 nanoparticles.

In contrast at 350 °C, roughly spherical shape with larger agglomerates of big particles formed from the coupling effect of the small nanoparticles. At 450 °C, thick but spherical and less agglomerated particles were formed. HRSEM micrograph shown in Fig. 3d for the samples calcined at 550 °C was spherical, more granular in nature and possesses a less dense structure. At 650 °C, closely packed spherical-shaped WO_3 nanoparticles were observed. In addition, it can be concluded that the growth of WO_3 nanoparticles leading to the formation of spherical shapes followed the conventional mechanism of Ostwald ripening and oriented attachment [33]. In this case, the WO_3 nuclei were formed from tungsten and plant extract precursors due to the annealing process. It is obvious that as the sintering temperature increases from 250 to 650 °C, the nanoparticles become more visible and the sizes of WO_3 nanoparticles also increase, while the rate of agglomeration reduces. It is noteworthy mentioning that the degree of porosity of the nanoparticles also reduced with temperature except at 550 °C possibly due to the destruction of the hollow

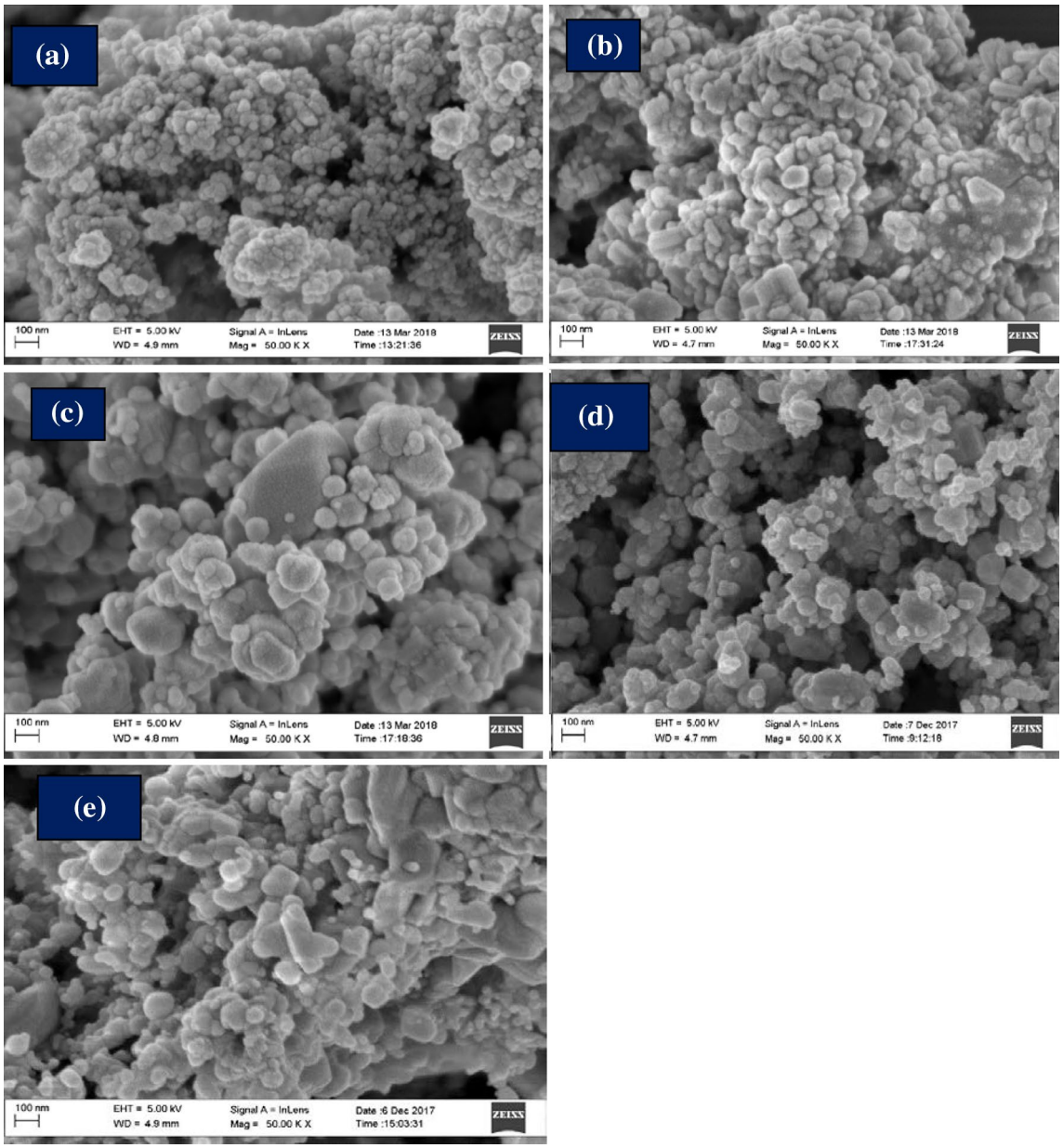

Fig. 3 HRSEM images of WO_3 nanoparticles prepared at optimum pH of 1 and calcined at temperature **a** 250 °C, **b** 350 °C, **c** 450 °C, **d** 550 °C, and **e** 650 °C at constant holding time of 2 h

structure. Between calcination temperatures of 350–550 °C, it was observed that the porous structure gradually disappeared and the crystallites' growth of WO_3 becomes more visible. In addition, it can be seen from these micrographs that the morphology and crystallite sizes' arrangement of the nanoparticles were a function of the applied temperature. For instance, the size of the WO_3 nanoparticles calcined at 250 °C was found to be in the range of 13.9–14.5 nm. While for the sample calcined between 350 and 450 °C, the particle size was in the range of 15.3–28.0 nm. A similar trend of large grain sizes between 27.8 and 36.0 nm was observed for the sample calcined between 550 and 650 °C. The direct linear relationship between the particle size and calcination temperature may be linked to the stepwise disappearance of crystal defects resulting to the formation of highly crystalline WO_3 nanoparticles [5]. These findings are in good agreement with the crystallite size obtained from the XRD analysis. Zhao and Miyauchi [53] reported that the morphology of synthesized WO_3 nanoparticles was dependent on calcination temperature. For instance, Zhao and colleague obtained discrete bowl-like hollow sphere for WO_3 calcined at 180 °C, solid spheres at 140 °C, and plate-like structures

at 100 °C and attributed the difference in morphological arrangement to the reduction in agglomeration as a function of calcination temperature. The results indicated that appropriate optimization of calcination temperatures is crucial to control the size and shape of the WO_3 nanoparticle. This is because low temperature may not be sufficient to reduce the tungsten hydrolysis products to the metallic state, while a too high temperature will cause rapid nucleation and coagulation of particles [51].

3.1.2 Elemental composition of the WO_3 nanoparticles synthesized at different pH values

EDS analysis was done to investigate elemental composition of the synthesized WO_3 nanoparticles at various pH values. The principle energy lines of all the elements seen on EDS spectra of the WO_3 synthesized at various pH values and annealing temperatures are shown in Fig. 4. The EDS spectrum indicates the synthesized materials composed of mainly W and O, as shown in Fig. 4, while other elements such as Mg, Ca, and K were present as impurities at different binding energies.

Figure 4 shows that the percentage of W at pH 1 was about 78% which is slightly higher than at other pH values. For pH 7, 10, and 13, other elements such as calcium, potassium, and magnesium were present, which suggest contamination of the WO_3. These elements were not detected at pH 4; however, the atomic percentage of W was lower than at pH 1. The EDS analysis confirmed that the as-synthesized materials under acidic conditions were pure due to the absence of other elements. Thus, pH 1 was chosen as the optimal pH to synthesize WO_3 nanoparticles from ammonium paratungstate, ($(NH_4)_{10}W_{12}O_{41}\cdot 5H_20$) and *Spondias mombin* plant extract. The C detected in the sample may originate from the carbon holey grids used to hold the sample or the plant extract.

3.1.3 XRD analysis of WO_3 nanoparticles synthesized at different pH

X-ray diffraction analysis was done to determine the crystal structure and the crystallite size of the as-prepared WO_3 nanoparticles at different pH solutions. Figure 5 illustrates XRD diffraction patterns of WO_3 nanoparticles synthesized at various pH values.

The XRD spectra for materials obtained at pH 1, 4, 7, and 10 demonstrated the presence of three intense diffraction peaks at 2θ values of 23.18°, 23.66°, and 24.38° with their corresponding crystal planes of (002), (020), and (200). The as-produced WO_3 nanoparticles were assigned body-centered tetragonal which is in agreement with the Joint Committee on Powder Diffraction Standards (JCPDS No 83–0951) for monoclinic structure and further confirmed that the obtained material exists in a single phase [33]. The intensity of the (002) facets was much stronger than that of the other facets observed in the XRD spectrum, which implies that the crystals were mainly dominated by the (002) facet and major growth existed in that direction. On the contrary, for sample prepared at pH 13, the peaks are not well resolved and not fully developed but the XRD shows a degree of crystalline material with peaks corresponding to the previous measurements, which meant that no WO_3 nanoparticles were produced at pH 13 or probably amorphous phase was produced instead of crystalline. The XRD results in Fig. 5 shows the presence of clear, sharp and intense diffraction peaks as well as increase in the Full Width at Half Maximum (FWHM) irrespective of the solution pH except for materials synthesized at pH 13 with not well resolved peaks. Furthermore, it was noticed that the crystal growth of the WO_3 structures preferentially oriented along the (002) direction, and according to Debye–Scherrer's formula, the average crystallite size calculated for materials prepared at pH 1, 4, 7, and 10 were 7.1, 14.7, 28.30, and 38.90 nm,

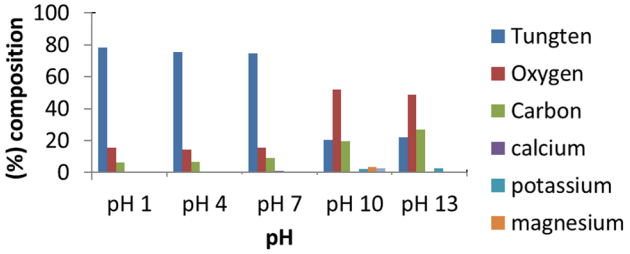

Fig. 4 Elemental composition of WO_3 nanoparticles prepared at different pH values

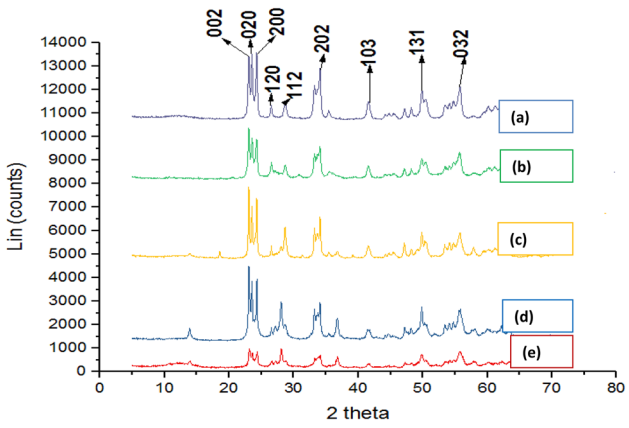

Fig. 5 XRD patterns of WO_3 nanoparticles prepared by optimizing at **a** pH 1, **b** pH 4, **c** pH 7, **d** pH 10, and **e** pH 13

respectively. The XRD results revealed that the crystalline size increased with increasing solution pH. The particle size calculated from XRD results match well with the HRSEM results. This similarity in sizes could be due to increment in coalescence and coagulation process under the applied acidic and alkaline medium. Kavitha et al. [19] reported an average size of 42 nm for the biosynthesized WO_3 nanoparticles based on *Fusarium solani* fungus extract in an acidic pH region. The particle size obtained by Kavitha and colleague is, however, seven times greater than the size obtained at pH 1 in this study and the differences in the particle size may be attributed to the nature of the reducing agents and other applied environmental conditions. Gu et al. [13] reported pH values over the range < 0.5, 1.0–1.4 and 1.5–2.0 for WO_3 nanoparticles, nanobundles and nanowires, respectively. Conclusively, the pH of 1 was taken as the optimum pH for this synthesis of WO_3 nanoparticles.

3.1.4 XRD analysis of WO_3 nanoparticles synthesized at different temperatures

Sintering temperature influences the nucleation and crystal growth which determined the morphology of the synthesized particles. As the calcination temperature is gradually increased, the adsorptive property of photocatalysts decreases, while the photocatalytic activity increases [20]. Therefore, the optimum calcination temperature which provides the moderate adsorptive capacity and excellent photocatalytic activity of the photocatalysts is required. On the other hand, further increase of calcination temperature decreases the photocatalytic performance of photocatalyst due to destruction of the hollow-crystalline structure [45]. The XRD patterns of the as-obtained materials at different annealed temperatures are shown in Fig. 6.

Studies have shown that WO_3 exists in different allotropic forms such as orthorhombic, triclinic, monoclinic, and hexagonal and that it fundamentally varies from each other

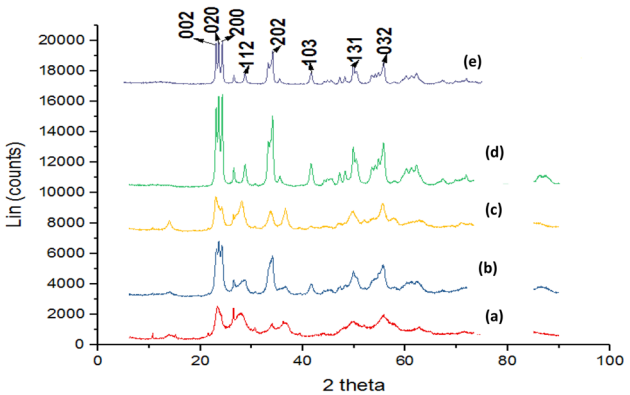

Fig. 6 XRD patterns showing WO_3 nanoparticles at an optimum pH of 1 calcined at **a** 250 °C, **b** 350 °C, **c** 450 °C, **d** 550 °C, and **e** 650 °C

based on the distortion of WO_6 octahedral [25]. However, in this present work, the diffraction peaks observed in the XRD pattern shown in Fig. 5 matched well to the crystal compositions of pure monoclinic polymorph of WO_3 (JCPDS No. 83–0951). The most dominant diffraction peaks appeared at 2θ values of 23.18°, 23.66°, and 24.38° with Miller indexes of (002), (020), and (200), respectively. The intensity of the diffraction peak with these miller indices is stronger than other crystal planes. The XRD results supported the results from morphological analysis, as shown in Fig. 3. It was observed that the intensity of the other diffraction peaks and the degree of crystallinity of WO_3 changed with increasing calcination temperature from 250 to 650 °C. Nevertheless, for the material calcined at 250 °C has broad diffraction peaks which further corroborated HRSEM results (see Fig. 3a). The broadening may be a result of many parameters like the change in particle size or due to instrumentation. In spite of the amorphous nature of the material, XRD results confirm that the as-synthesized materials at this temperature are in good agreement with the standard JCPDS card No. 83–0951 for monoclinic structure of WO_3 [33]. This shows that the calcination temperature influenced the crystallization and nucleation of the material prepared without necessarily causes phase changes. The average crystalline sizes of WO_3 nanoparticles prepared at different temperatures were calculated by Debye–Scherrer's formula. The average crystalline size was found to be 13.1, 14.7, 25.2, 27.1, 29, and 31 nm for WO_3 nanoparticles calcined at 250°, 350°, 450°, 550°, and 650 °C. The broadening of diffraction peaks at 250 °C may be responsible for the observed relatively small crystallite size compared to others. It can be noticed that there is a direct linear relationship between the crystallites size and the calcination temperatures. The observed trend closely agrees with the previous findings on the WO_3 samples prepared by different workers with different synthetic techniques especially electrochemical deposition technique and a gas evaporation method [9, 33]. This suggests that the calcination temperature affects the particle size of the materials, however, thereby enhanced its crystalline nature. With an increase in calcination temperature from 350 to 650 °C, the relative intensity of the peaks increases, while the degree of peak broadness reduces. The presence of sharper and intense peaks as a function of calcination temperature is an indication of good crystallinity of the prepared materials and by extension the observed increasing size of the particles. Similarly, Bamwenda and Arakawa [3] opined that the presence of clear sharp peaks due to temperature increment was an evidence of disappearance of crystal defects and enhancement of crystallinity and particle sizes. In the same vein, Jin and Liu [16] found that the crystallite sizes also increase with increasing in calcination temperature from 41.9 nm at 200 °C to 47. 1 nm at 600 °C. Conversely, Sun et al. [43] and Prabhu et al. [37] independently reported a reduction

of crystallite size upon increase in calcination temperature for WO_3 samples prepared by spray pyrolysis method and solvothermal chemical method. The authors attributed the decrease in the crystallite sizes to the destruction of the hollow structures of WO_3 at higher temperature. It is logical to conclude that these differences in the particle size may be due to the different synthetic methods employed.

3.2 BET results for the synthesized WO_3 nanocomposites

The surface area of the synthesized WO_3 nanoparticles at different pH and calcination temperature was determined using multiple-plot BET analysis. Table 2 shows the surface area for the synthesized nanomaterials in comparison with the commercial WO_3.

According to Table 2, it is obvious that the BET surface area of WO_3 nanoparticles prepared at pH 1 is higher than other pH values. This means that the surface area of WO_3 reduces with increasing pH and may be ascribed to the supersaturation process followed by homogeneous nucleation in the acidic medium than neutral and alkaline pH, respectively. In addition, the higher surface area obtained for material prepared at pH 1 can be ascribed to a higher rate of electron transfer in an acidic medium than in a neutral or basic medium. In general, WO_3 is known as a low surface area material; for instance, Rajagopal et al. [38] reported BET surface area of 11.1 m^2/g for synthesized WO_3 nanoparticles by simple chemical precipitation method of tungstic acid and sodium hydroxide under acidic region. Mu et al. [33] obtained BET surface area of 19.42 m^2/g for WO_3 prepared by a low-temperature hydrothermal method containing $Na_2WO_4{\cdot}2H_2O$ precursor. It was noticed that the surface area obtained in this study irrespective of the pH is higher than the commercial type and even the reported value in the literature. The possible reasons may be linked to the method of synthesis and nature of the tungsten precursor. In this study, where green synthesis was used, the plant extracts probably capped and stabilized the WO_3 nuclei during growth, thereby enhanced its surface area. The high surface area can also be linked to the doping effect of carbonaceous species from the polyphenolic in the *Spondias mombin* aqueous leaves' extract. Furthermore, it can be seen from Table 2 that calcination temperature influenced the specific surface area of the WO_3 particles. As shown in Table 2, the BET surface area increased with increasing calcination temperature and may be attributed to the fast nucleation process which aided the transformation of WO_3 from amorphous to crystalline form. This shows that BET surface area of WO_3 nanoparticles is directly proportional to calcination temperature, but inversely related to the solution pH.

Table 2 Surface areas of WO_3 nanoparticles prepared at different solution pH and calcination temperature

Solution pH	Surface area (m^2/g)	Calcination temperature (°C)	Surface area (m^2/g)
1	352.59	250	156.34
4	331.45	350	212.56
7	245.12	450	337.29
10	223.67	550	352.59
13	15.78	650	18.13
Commercial WO_3	19.42		

3.3 XPS analysis for the synthesized WO_3 nanomaterials

The chemical composition and oxidation state of W and O in synthesized WO_3 at optimum pH and sintering temperature were examined by XPS. Figure 7a depicts the general XPS survey of WO_3, and it was noticed that the material prepared contained W, O, and C elements at different binding energies and theirs corresponding orbital types were 4f, 1 s, and 1 s, respectively. The high-resolution XPS scan of the W (4f) core level (Fig. 7b) shows the doublet peaks with binding energies of 35.6 eV and 37.6 eV which correspond to $W4f_{7/2}$ and $W4f_{5/2,}$ respectively. It should be mentioned that the detailed W scan in Fig. 7b is typical for all specimens and that there were relative small changes in the ratios between the stoichiometric and nonstoichiometric W. This ratio was approximately 4:1 except for the synthesized WO_3 nanoparticles at pH 13. The energy positions suggested that W existed in oxidation states of + 6 [26]. Another set of double peaks though of low intensity at binding energies of 34.9 and 37.0 eV were assigned W in 5 + oxidation state. However, the peaks' intensity of W^{6+} outweighs that of W^{5+}. Figure 7c depicts the deconvoluted XPS scan of the O 1 s region of WO_3 and one prominent peak was noticed at the binding energy of 530.5 eV and corresponds to the lattice oxygen in the form of (O^{2-}). In the same vein, peaks of low intensity were found at the binding energies of 532. 5 eV and 533.1 eV were assigned absorbed oxygen and Wi–O bond, respectively. Based on the XPS spectra, it is logical to conclude that W (4f) and O (1 s) peaks with binding energies at 35.7 eV and 530.5 eV agreed well with WO_3 nanoparticles reported in the literature [38].

4 Conclusion

In summary, WO_3 nanoparticles with controllable morphologies and sizes were synthesized from ammonium paratungstate, $(NH_4)_{10}W_{11}O_{41}{\cdot}5H_2O$) and *Spondias mombin* aqueous extract by a simple, low-cost, and appropriate green route. Besides, solution pH and calcination temperature played a

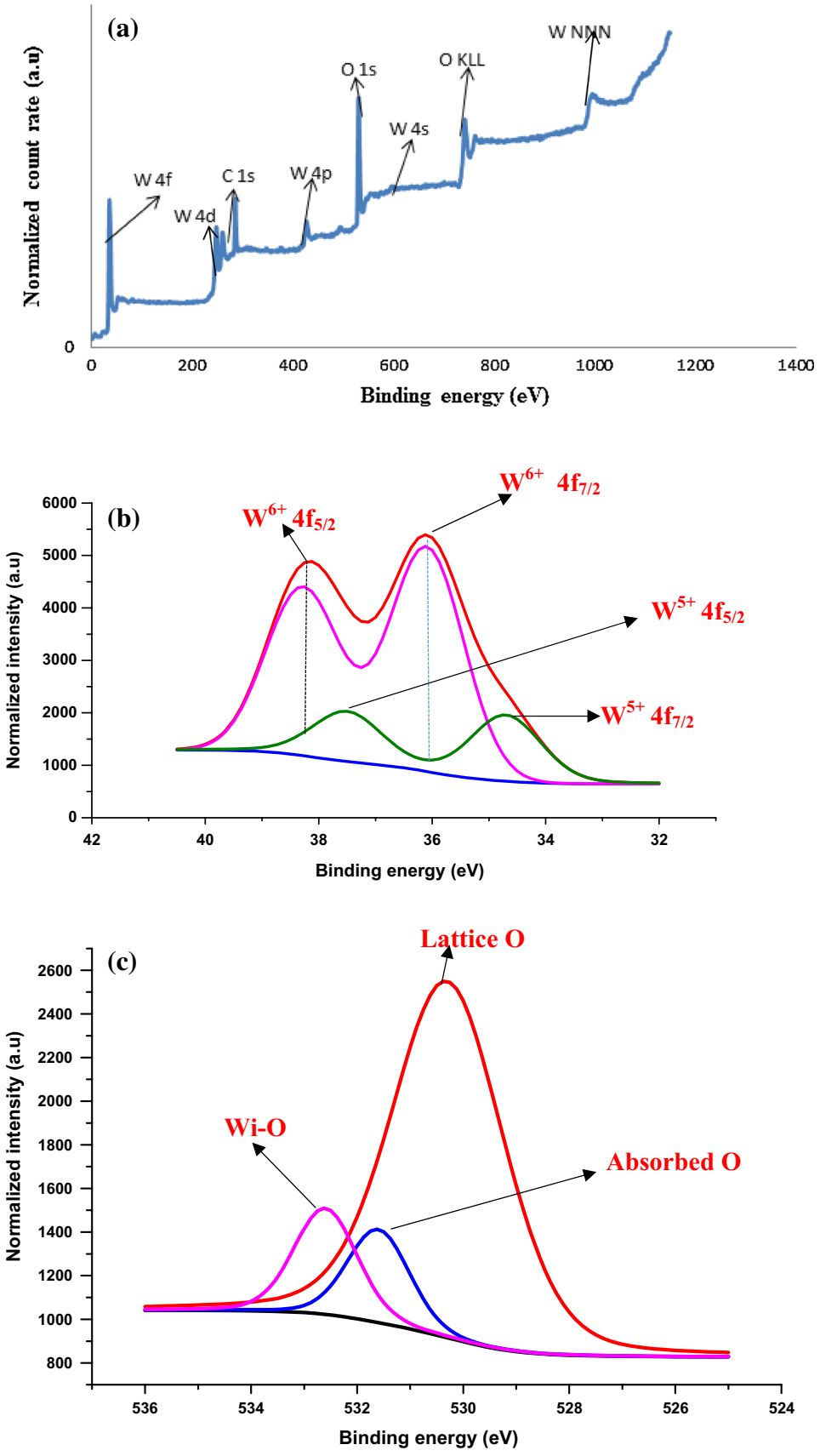

Fig. 7 **a** XPS survey of green-synthesized WO_3 nanoparticles. **b** XPS survey W ($4f_{7/2}$) and ($4f_{5/2}$) photoelectronic peak. **c** XPS survey O (1 s) region

crucial role in the morphological arrangement and structural properties such as average crystallite size and surface area. It was established that crystallite sizes increase with solution pH and calcination temperature. There was no alteration of WO_3 phase type under the applied solution pH and calcination temperatures, instead only monoclinic polymorph was obtained. An acidic medium favours the formation of pure monoclinic symmetry of WO_3. In conclusion, all characterization techniques employed in the present work confirmed successful synthesis and formation of monoclinic phase of WO_3 nanoparticles with higher specific surface area and small crystal size compared to other preparation techniques in the literature.

Acknowledgements The authors acknowledge the financial assistance received from Tertiary Education Tax Fund (TETFUND) Nigeria with Grant number TETFUND/FUTMINNA/NRF/2017/02 is highly commendable. The authors remain grateful to the following; Prof.. W.D. Roos for (XPS analysis, University of the Free State, South Africa), Dr. Remy Bucher (XRD, ithemba Labs), and Dr. Franscious Cummings [HRTEM, Physics department, University of the Western Cape (UWC), South Africa].

Compliance with ethical standards

Conflict of interest The authors declared no conflicts of interest.

References

1. I.O. Ademola, B.O. Fagemi, S.O. Idowu, Anthelminthic activity of extract of *Spondias mombin* against gastro intestinal nematodes of sheep: Studies *in-vitro* and i*n-vivo*. Trop. Anim. Health Prod. **37**(3), 223–235 (2005)
2. M.K. Aminian, Morphology influence on photocatalytic activity of tungsten oxide loaded by platinum nanoparticles. J. Mater. Res. **25**(1), 141–148 (2009)
3. G.R. Bamwenda, H. Arakawa, The visible light induced photocatalytic activity of tungsten trioxide powders. Appl. Catal. A **210**(1–2), 181–191 (2001)
4. M.S. Bazarjani, M. Hojamberdiev, K. Morita, G. Zhu, G. Cherkashinin, C. Fasel, T. Herrmann, H. Breitzke, A. Gurlo, R. Riedel, Visible light photocatalysis with c-$WO_{(3-x)}$/WO_3xH_2O nano-heterostructures *in-situ* formed in mesoporous polycarbosilane-siloxane polymer. J. Am. Chem. Soc. **135**, 4467–4475 (2013)
5. M.M.H. Bhyuiyan, T. Ueda, T. Ikegami, K. Ebihara, Gas sensing properties of metal doped WO_3 thin film sensors prepared by pulsed laser deposition and DC sputtering process. Jpn. J. Appl. Phys. **45**(1), 8469–8472 (2006)
6. C. Chang, M. Yang, H. Wen, J. Chern, Estimation of total flavonoid content in propolis by two complementary colorimetric methods. J. Food Drug Anal. **10**, 178–182 (2002)
7. R.P.S. Chauhan, C. Gupta, D. Prakash, Methodological advancements in green nanotechnology and their applications in biological synthesis of herbal nanoparticles. Int. J. Bioassays **1**(7), 6–10 (2012)
8. N. Cicco, M. Lanorte, M. Paraggio, M. Viggiano, V. Lattanzio, A reproducible, rapid and inexpensive Folin-Ciocalteu micro-method in determining phenolics of plant methanol extracts. Microchem. J. **91**(1), 107–110 (2009)
9. M.K Deepa, T.N. Suryaprakash, K. Pawan, Green synthesized silver nanoparticles. J. Chem. Pharm. Res. **8**(1), 411–419 (2016)
10. A.D. Dwivedi, K. Gopal, Biosynthesis of silver and gold nanoparticles using Chenopodium album leaf extract. Colloids Surf. A **369**, 27–33 (2010)
11. C. Feng, S. Wang, B. Geng, Titanium (IV) doped WO_3 nanocuboids: Fabrication and enhanced visible-light-driven photocatalytic performance. Nanoscale **3**, 3695–3699 (2011)
12. F.D. Fonzo, A. Bailini, V. Russo, A.A. Baserga, A. Cattaneo, M.G. Beghi, P.M. Ossi, C.S. Casari, A.L. Bassi, C.E. Bottani, Synthesis and characterization of tungsten and tungsten oxide nanostructured films. Catal. Today **116**(1), 69–73 (2006)
13. Z. Gu, H. Li, T. Zhai, W. Yang, Y. Xia, Y. Ma, J. Yao, Large-scale synthesis of single-crystal hexagonal tungsten trioxide nanowires and electrochemical lithium intercalation into the nanocrystals. J. Solid State Chem. **180**, 98–105 (2007)
14. O.M. Hussain, A.S. Swapnasmitha, J. John, R. Pinto, Structure and morphology of laser-ablated WO_3 thin films. J. Appl. Phys. A **81**(6), 291–1297 (2005)
15. A.: Vacuum, Visible light-induced photocatalytic properties of WO_3 films deposited by dc reactive magnetron sputtering. J. Vac. Sci. Technol. Surf. Films **30**(3), 5082–5086 (2012)
16. S.Q. Jin, G.H. Liu, Preparation and photocatalytic activity of fluorine doped WO_3 under UV and visible light. Dig. J. Nanomater. Biostruct. **4**(11), 1179–1188 (2016)
17. A.A. Joraid, S.N. Almari, Effect of annealing on structural and optical properties of WO_3 thin films prepared by electron-beam coating. Phys. B **391**(2), 199–205 (2007)
18. M. Karthik, M. Parthibavarman, A. Kumaresan, S. Prabhakaran, V. Hariharan, R. Poonguzhali, S. Sathishkumar, One-step microwave synthesis of pure and Mn doped WO3 nanoparticles and its structural, optical and electrochemical properties. J. Mater. Sci. **28**(9), 1–8 (2016)
19. N.S. Kavitha, K.S. Venkatesh, N.S. Palani, R. Ilangovan, Fungus mediated biosynthesis of WO_3 nanoparticles using *Fusarium solani* extract. Am. Inst. Phys. Conf. Proc. **1832**, 050130 (2017)
20. T.J. Kemp, R.A. Mcintyre, Transition metal-doped titanium(IV) dioxide: characterization and influence on photodegradation of poly(vinyl chloride). Polym. Degrad. Stab. **91**(1), 165–194 (2006)
21. S. Komaba, N. Kumagai, K. Kato, H. Yashiro (2000). Hydrothermal synthesis of hexagonal tungsten trioxide from Li_2WO_4 solution and electrochemical lithium intercalation into the oxide, Solid State Ionics **135**, 193–197
22. X. Li, H. Xu, Z.S. Chen, G. Chen, Biosynthesis of nanoparticles by microorganisms and their applications. J. Nanomater. **2011**, 270974 (2011)
23. Q.H. Li, L.M. Wang, D.Q. Chu, X.Z. Yang, Z.Y. Zhang, Cylindrical stacks and flower-like tungsten oxide microstructures: controllable synthesis and photocatalytic properties. Ceram. Int. **40**(3), 4969–4973 (2014)
24. Z. Liu, Y. Bando, C. Tang, Synthesis of tungsten oxide nanowires. Chem. Phys. Lett. **372**, 179–182 (2003)
25. H. Liu, T. Peng, D. Ke, Z. Peng, C. Yan, Preparation and photocatalytic activity of dysprosium doped tungsten trioxide nanoparticles. Mater. Chem. Phys. **104**, 377–383 (2007)
26. Y. Liu, Y. Li, W. Li, S. Han, C. Liu, Photoelectrochemical properties and photocatalytic activity of nitrogen-doped nanoporous WO_3 photoelectrodes under visible light. Appl. Surf. Sci. **258**(12), 5038–5045 (2012)
27. Y. Liu, Q. Li, S. Gao, J.K. Shang, Template-free solvothermal synthesis of WO3/WO3·H2O hollow spheres and their enhanced photocatalytic activity from the mixture phase effect. Cryst. Eng. Commun. **16**, 7493–7501 (2014)

28. J. Lin, P. Hu, Y. Zhang, M. Fan, Z. He, C.K. Ngaw, J.S.C. Loo, D. Liao, T.T.Y. Tan, Understanding the photo electrochemical properties of a reduced graphene oxide-WO_3 heterojunction photo anode for efficient solar light- driven overall water splitting. R. Soc. Chem. Adv. **3**, 9330–9336 (2013)
29. E. Luevano-Hipolito, A. la Cruz, E. Lopez-Cuellar, Q.L. Yu, H.J.H. Brouwers, Synthesis, characterization and photocatalytic activity of WO_3/TiO_2 for NO removal under UV and visible light irradiation. Mater. Chem. Phys. **148**, 208–213 (2014)
30. A.H. Mahan, P.A. Parilla, K.M. Jones, A.C. Dillon, Hot-wire chemical vapor deposition of crystalline tungsten oxide nanoparticles at high density. Chem. Phys. Lett. **413**(1), 88–94 (2005)
31. A. Mahshad, M.A. Reza, R. Alimorad, Preparation of different WO_3 nanostructures and comparison of their ability for congo red photo degradation. Iran. J. Chem. Chem. Eng. **31**(1), 31–38 (2012)
32. A.K. Mittal, Y. Chisti, C. Banerjee, Synthesis of metallic nanoparticles using plant extracts. Biotechnol. Adv. **31**, 346–356 (2013)
33. W. Mu, X. Xie, X. Li, R. Zhang, Q. Yu, K. Lv, H. Wei, Y. Jian, Characterizations of Nb-doped WO_3 nanomaterials and their enhanced photocatalytic performance. R. Soc. Chem. **4**, 36064–36070 (2014)
34. T.A. Nguyen, T.S. Jun, M. Rashid, Y.S. Kim, Synthesis of mesoporous tungsten oxide nanofibers using the electrospinning method. Mater. Lett. **65**(17–18), 2823–2825 (2011)
35. E.S. Omoregie, E.I. Oikeh, Comparative studies on the phytochemical composition, phenolic content and antioxidant activities of methanol leaf extracts of *Spondias mombin* and *Polyathia longifolia*. Jordan J. Biol. Sci. **8**(2), 145–149 (2015)
36. T. Peng, D. Ke, J. Xiao, L. Wang, J. Hu, L. Zan, Hexagonal phase WO_3 nanorods: Hydrothermal preparation, formation mechanism and its photocatalytic O_2 production under visible-light irradiation. J. Solid State Chem. **194**, 250–256 (2012)
37. N. Prabhu, S. Agilan, N. Muthukumarasamy, T.S. Senthil, Preparation and characterizations of copper doped WO_3 nanoparticles prepared by solvo-thermal cum chemical method. Int. J. Chem. Technol. Res. **6**(7), 3487–3490 (2014)
38. S. Rajagopal, D. Nataraj, D. Mangalaraj, Y. Djaoued, J. Robichaud, O.Y. Khyzhun, Controlled growth of WO_3 nanostructures with three different morphologies and their structural, optical, and photodecomposition studies. Nanoscale Res. Lett. **4**, 1335–1342 (2009)
39. M.C. Roa, O.M. Hussain, Growth and characterization of vacuum evaporated WO_3 thin films for electrochromic device application. Res. J. Chem. Sci. **1**(17), 92–95 (2011)
40. M. Sadakane, K. Sasaki, H. Kunioku, B. Ohtani, R. Abe, W. Ueda, Preparation of 3-D ordered macroporous tungsten oxides and nano-crystalline particulate tungsten oxides using a colloidal crystal template method, and their structural characterization and application as photocatalysts under visible light irradiation. J. Mater. Chem. **20**, 1811–1818 (2010)
41. H. Song, Y. Li, Z. Lou, M. Xiao, L. Hu, Z. Ye, L. Zhu, Synthesis of Fe-doped WO_3 nanostructures with high visible-light-driven photocatalytic activities. Appl. Catal. B Environ. **166–167**, 112–120 (2014)
42. J. Sungpanich, T. Thongtem, S. Thongtem, Photocatalysis of WO3 nanoplates synthesized by conventional-hydrothermal and microwave-hydrothermal methods and of commercial WO3 nanorods. J. Nanomater. **2014**, 739251 (2014)
43. M. Sun, N. Xu, Y.W. Cao, J.N. Yao, E.G. Wang, Nanocrystalline tungsten oxide thin film: Preparation, microstructure, and photochromic behavior. J. Mater. Res. **15**(4), 927–933 (2000)
44. S. Supothina, P. Seeharaj, S. Yoriya, M. Sriyudthsak, Synthesis of tungsten oxide nanoparticles by acid precipitation method. Ceram. Int. **33**, 931–936 (2007)
45. C. Suwanchawalit, S. Wongnawa, Influence of calcination on the microstructures and photocatalytic activity of potassium oxalate-doped TiO_2 powders. Appl. Catal. A **338**(2), 87–99 (2008)
46. K.N. Thakkar, S.S. Mhatre, R.Y. Parikh, Biological synthesis of metallic nanoparticles. Nanomed. Nanotechnol. Biol. Med. **6**, 257–262 (2010)
47. I. Vamvasakis, I. Georgaki, D. Vernardou, G. Kenanakis, N. Katsarakis, Synthesis of WO_3 catalytic powders: evaluation of photocatalytic activity under NUV/visible light irradiation and alkaline reaction pH. J. Sol-Gel Sci. Technol. **76**(1), 120–128 (2015)
48. J. Wang, E. Khoo, P.S. Lee, J. Ma, Controlled synthesis of WO_3 nanorods and their electrochromic properties in H_2SO_4 electrolyte. J. Phys. Chem. C **113**, 9655–9658 (2009)
49. Y. Wicaksana, S. Liu, J. Scott, R. Amal, Tungsten Trioxide as a Visible Light Photocatalyst for Volatile. Org. Carbon Remov. Mol. **19**, 17747–17762 (2014)
50. G. Xin, W. Guo, T. Ma, Effect of annealing temperature on the photocatalytic activity of WO_3 for O_2 evolution. Appl. Surf. Sci. **256**, 165–169 (2009)
51. L. Xiong, T. He, Synthesis and characterization of ultrafine tungsten and tungsten oxide nanoparticles by a reverse microemulsion-mediated method. Chem. Mater. **18**, 2211–2218 (2006)
52. Z. Yaakob, M. Pudukudy, R. Rajendran, Visible light active novel WO_3 nanospheres for methylene blue degradation. Der Pharma Chem. **5**(6), 208–212 (2013)
53. Z.G. Zhao, M. Miyauchi, Shape modulation of tungstic acid and tungsten oxide hollow structures. J. Phys. Chem. C **113**(16), 6539–6546 (2009)
54. Y. Zheng, G. Chen, Y. Yu, J. Sun, Y. Zhou, J. Pei, Template and surfactant free synthesis of hierarchical $WO_3 \cdot 0.33H_2O$ via a facile solvothermal route for photocatalytic RhB degradation. Cryst. Eng. Commun. **16**, 6107–6113 (2014)